

Quantitative Parametric Mapping of Tissues Properties from Standard Magnetic Resonance Imaging Enabled by Deep Learning

Yan Wu^{1,2,*}, Yajun Ma^{3,*}, Youngwook Kee², Nataliya Kovalchuk¹, Dante Capaldi¹, Hongyi Ren¹, Steven Hancock¹, Eric Chang³, Marcus Alley², John Pauly², Jiang Du^{3,*}, Shreyas Vasanawala^{2,*}, Lei Xing^{1,*}

¹Radiation Oncology Department, Stanford University, 875 Blake Wilbur Drive, G204, Stanford, California 94305

²Radiology Department, Stanford University, 300 Pasteur Drive, Stanford, California 94305

³Radiology Department, University of California San Diego, 9500 Gilman Drive, #0888, La Jolla, California 92093

* corresponding author

+ equal contribution

Summary

Magnetic resonance imaging (MRI) offers superior soft tissue contrast and is widely used in biomedicine. However, conventional MRI is not quantitative, which presents a bottleneck in image analysis and digital healthcare. Typically, additional scans are required to disentangle the effect of multiple parameters of MR and extract quantitative tissue properties. Here we investigate a data-driven strategy Q^2MRI (Qualitative and Quantitative MRI) to derive quantitative parametric maps from standard MR images without additional data acquisition. By taking advantage of the interdependency between various MRI parametric maps buried in training data, the proposed deep learning strategy enables accurate prediction of tissue relaxation properties as well as other biophysical and biochemical characteristics from a single or a few images with conventional T_1/T_2 weighting. Superior performance has been achieved in quantitative MR imaging of the knee and liver. Q^2MRI promises to provide a powerful tool for a variety of biomedical applications and facilitate the next generation of digital medicine.

Introduction

MRI exploits the magnetic properties of tissues and provides noninvasive imaging of the human body for a wide variety of clinical applications [1]. While adopted ubiquitously, current MRI techniques cannot directly evaluate inherent physical properties of tissue (e.g., T_1 or T_2 relaxation times), which presents a bottleneck in image analysis and precision medicine [2]. The signal intensity of an MR image depends not only on tissue properties themselves, but also acquisition parameters (e.g., time of repetition, echo time, flip angle) and condition of the MR system being used (e.g., homogeneities of the radiofrequency field B_1 and main magnetic field B_0 , uniformity of receiver coil sensitivity). In general, the MRI parameter space can be divided into three subspaces, corresponding to the tissue relaxation properties, the acquisition parameters, and the system conditions (Fig. 1a). Conventionally, an MR image is acquired by using a pre-selected pulse sequence with specific imaging parameter setting, and the resulting image is qualitative in nature, with its signal intensity being a function of both tissue properties and other factors in the MRI parameter space. In order to derive a quantitative parametric map that reflects only a tissue property, one has to perform multiple samplings in the acquisition parameter subspace and then solve the system equations.

In past decades, extensive research efforts have been devoted to finding effective means to rapidly explore the multi-parametric space for quantitative MR imaging. A conventional approach quantifies a single tissue relaxation parameter by extracting the exponential decay/regrowth rate from multiple measurements (Fig. 1b) [3-7]. This strategy requires a substantially long scan time and is prone to system imperfections. Magnetic/radiofrequency field maps are sometimes measured to compensate for inaccuracy caused by field inhomogeneities [8-10]. Moreover, advanced image reconstruction techniques, such as compressed sensing and low rank processing, can be incorporated into quantitative MRI [11-14]. Then multi-parametric mapping methods have been developed, such as MR fingerprinting, MAGiC, multi-tasking, and EPTI [15-23]. With the help of advanced parameter fitting techniques, various tissue relaxation properties and field maps can be simultaneously estimated from the same input images (Fig. 1c). However, special pulse sequences are required. Recently, deep learning [24] has been employed to accelerate the data acquisition or post-processing in quantitative parametric mapping [25, 26] (as well as in other medical imaging applications [27]). Despite these remarkable speed-ups, additional scans are always required, hindering widespread adoption of quantitative MRI in clinical practice.

Here, we report a data-driven solution for quantitative measurement of inherent tissue properties with automatic compensation for system imperfections. Fundamentally different from previous approaches, the Q^2MRI technique leverages deep learning to exploit the inherent relationship within and across MRI parameter subspaces to derive quantitative parametric maps from standard MRI acquisitions. In our process, a significant portion of the information needed for parametric mapping is obtained from training data acquired using different pulse sequences. As a result, it

becomes possible to predict tissue relaxation properties and field maps from a routine MRI examination without additional data acquisition or change of clinical workflow (Fig. 1d). Furthermore, biophysical and biochemical parametric maps — traditionally obtained with the involvement of confounding models (e.g., quantitative susceptibility map and proton density fat fraction map [28, 29]) — can be derived from the same framework without further processing. In this sense, the proposed strategy goes beyond the scope of multi-parametric mapping for relaxation properties. Applications of Q^2MRI to the knee and liver show that the proposed technique provides an accurate and efficient way for quantitative MR imaging.

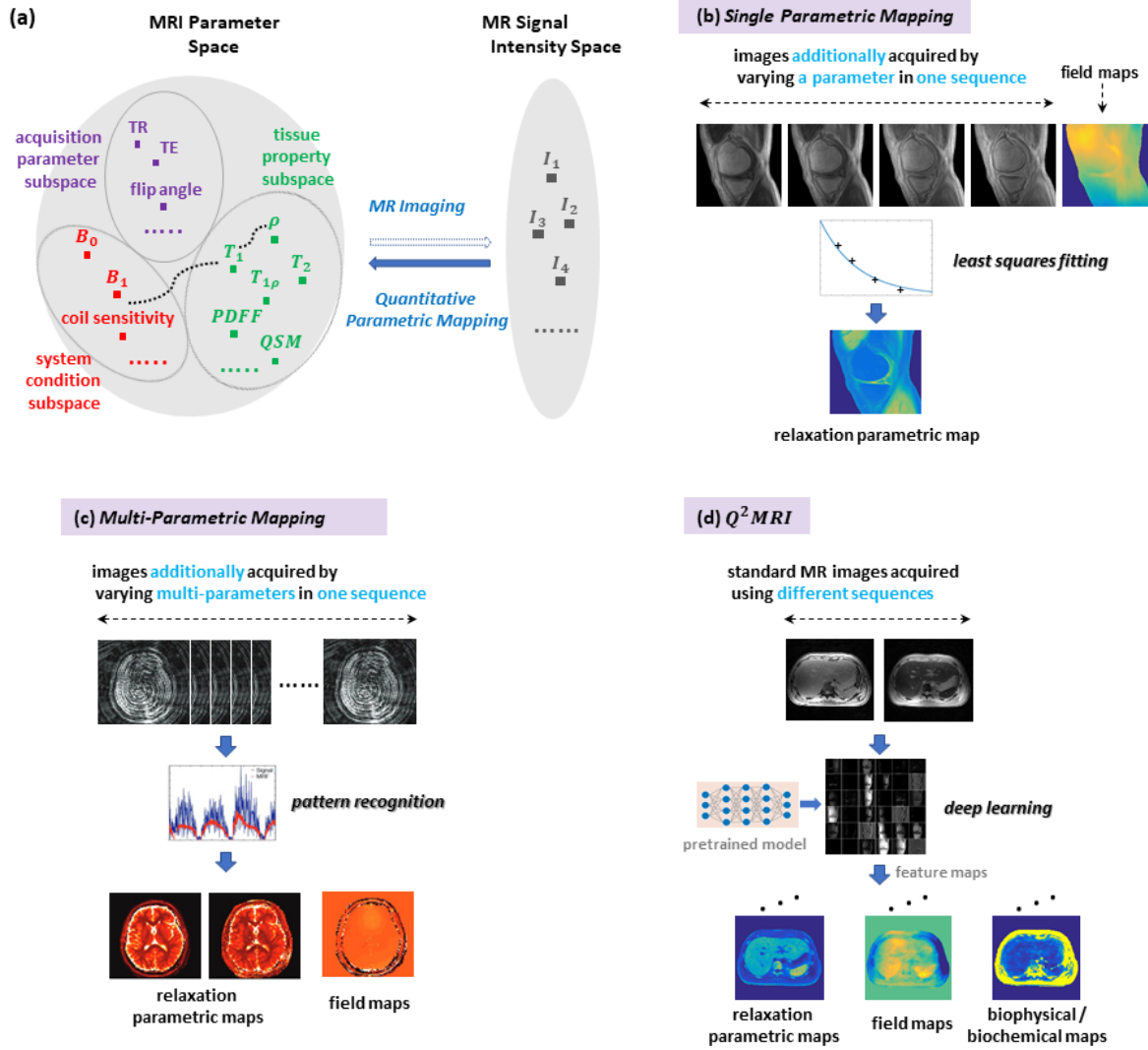


Figure 1. An illustration of conventional and proposed quantitative parametric mapping strategies. (a) The MRI parameter space consists of three subspaces, representing tissue properties, acquisition parameters, and system conditions, respectively. Quantitative parametric mapping can be achieved by sampling the acquisition parameter subspace and then solving the inverse problem from multiple measurements. (b) In single parametric mapping, a quantitative tissue relaxation parametric map (e.g., T_1) is extracted from several images acquired using the same pulse sequence but different acquisition parameters (e.g., flip angle), and the result is further compensated by field map (e.g., B_1). Here, the field map is specifically measured, and parameter quantification is typically implemented using least squares fitting. (c) In multi-parametric mapping (e.g., MR fingerprinting), a series of images is acquired using a specially designed pulse sequence with variations in multiple acquisition parameters (e.g., repetition time, echo time, and flip angle); subsequently, tissue relaxation properties (T_1 , T_2) and field maps (B_0 , B_1) are simultaneously estimated using advanced parameter fitting techniques (e.g., pattern recognition). (d) In the proposed Q^2MRI method, tissue relaxation properties (e.g., T_1 , T_2) and field maps (e.g., B_0 , B_1) are derived from one or a few MR images with conventional T_1/T_2 weighting, which are obtainable in clinical practice. Other biophysical and biochemical parametric maps (e.g., proton density fat fraction map) can also be derived in the same deep learning framework without further processing. The essence of the proposed method is to use deep learning to exploit *a priori* information on various parameters in the MRI parameter space (within/across different subspaces), mitigating the need to make actual measurements as is required by parameter quantification.

Results

In this study, Q^2MRI was validated in T_1 and T_2^* mapping of the knee, and in R_2^* mapping of the liver, where deep neural networks were used to provide end-to-end mappings. In the knee, T_1 , ρ , and B_1 maps were predicted from single T_1 -

weighted images, and T_2^* maps were derived from single T_1 - and T_2^* -weighted images. In the liver, R_2^* , B_0 , and proton density fat fraction ($PDFF$) maps were estimated from pairs of in-phase and out-of-phase images (Fig. 2).

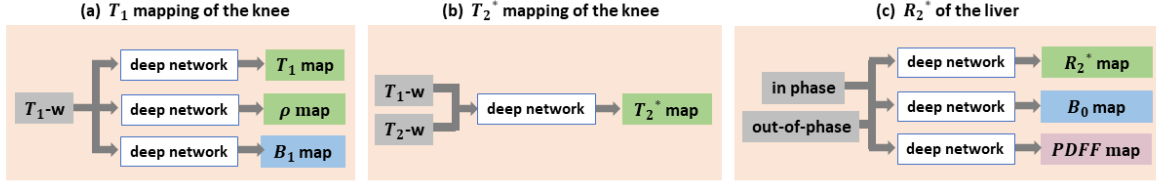


Figure 2. In Q^2MRI , deep learning models are trained to provide end-to-end mapping from single images to quantitative parametric maps and field maps.

T_1 and T_2^* Mapping of the Knee

For T_1 mapping of the knee, T_1 , ρ , and B_1 maps were predicted from single T_1 -weighted images. Here, the ground truth T_1 map was extracted from four T_1 -weighted images (acquired using variable flip angles of 5° , 10° , 20° , and 30° , respectively) via least squares fitting, and further corrected by the measured B_1 map; ρ map was calculated from a T_1 -weighted image and T_1 map. The input image was one of the four T_1 -weighted images (acquired using a specific flip angle of 5° , 10° , 20° , or 30°). A total of 1224 two-dimensional (2D) images from 59 subjects (including 50 osteoarthritis patients and 9 healthy volunteers) were used for training and testing, with six-fold cross-validation applied.

High fidelity mapping was achieved consistently across patients. A representative case is shown in Fig. 3. In the resultant T_1 maps, compensation for B_1 inhomogeneity was automatically achieved without use of a measured B_1 map. It is intriguing that the accurately predicted B_1 map was implicitly incorporated into the T_1 mapping models, which mitigated the need for actual B_1 measurement. On the individual pixel level, high correlation coefficients, low l_1 errors and high SSIM were obtained for various maps that were derived from different input images (Table 1). We note that slightly higher accuracy was achieved from input images that had been acquired using a flip angle of 20° or 30° , where T_1 effect was more prominent. Within the regions of interest (ROIs) in femur, tibia, and patella cartilage (which were manually segmented), averaged T_1 was calculated; the Bland-Altman plots are shown in Fig. 4.

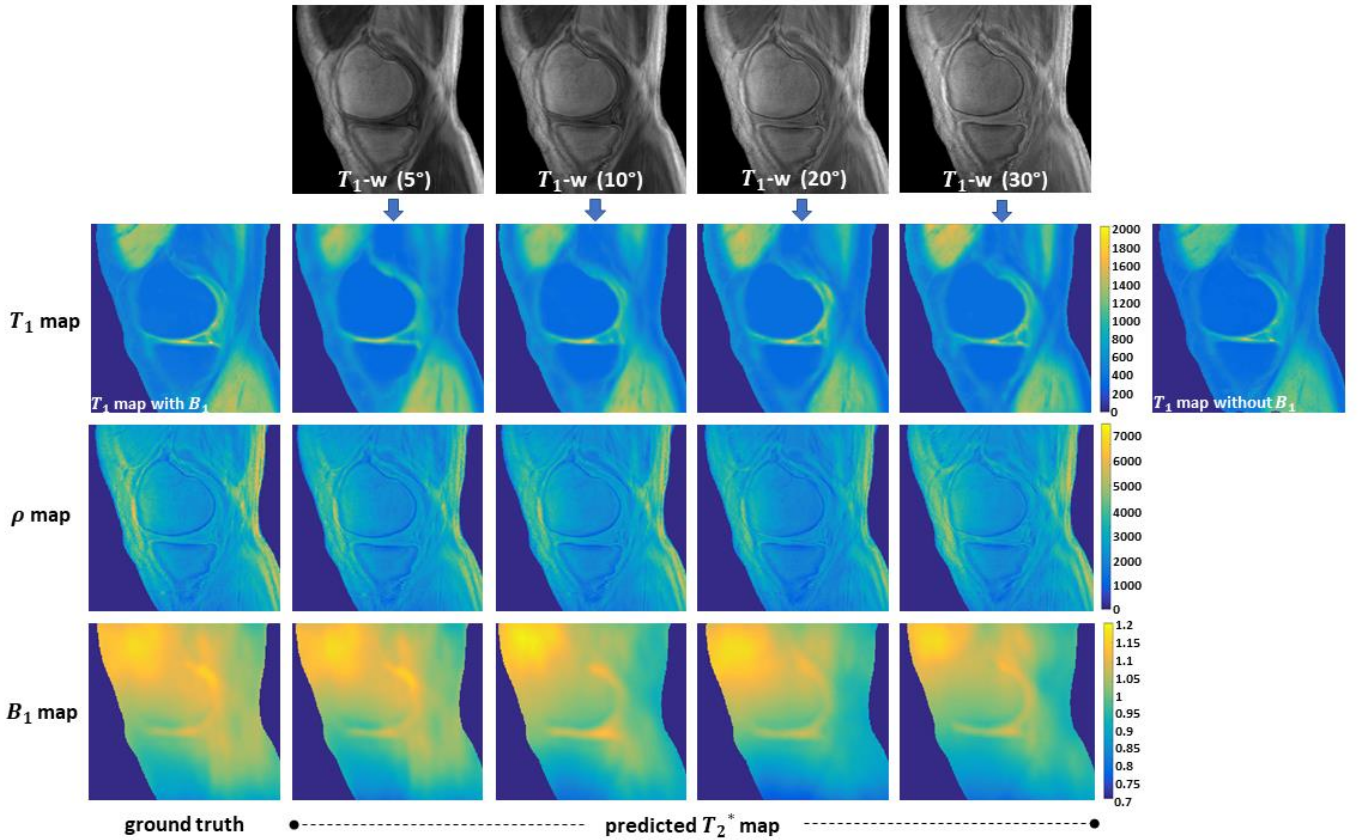


Figure 3. Prediction of T_1 , ρ , and B_1 maps of the knee from single T_1 -weighted images acquired using a specific flip angle (5° , 10° , 20° , and 30° respectively). The quantitative parametric maps and field maps predicted from different input images are all very close to the ground truth maps. Particularly in the resultant T_1 maps, compensation for B_1 inhomogeneity is automatically achieved without use of the measured B_1 map.

Input image		T_1 w (5°)	T_1 w (10°)	T_1 w (20°)	T_1 w (30°)
Output map					
T_1 map	l_1 Error	0.1026 ± 0.0311	0.0986 ± 0.0311	0.0952 ± 0.0283	0.0937 ± 0.0304
	Correlation	0.9681 ± 0.0276	0.9749 ± 0.0185	0.9778 ± 0.0170	0.9786 ± 0.0160
	$SSIM$	0.7743 ± 0.0430	0.7862 ± 0.0338	0.8151 ± 0.0303	0.8225 ± 0.0262
ρ map	l_1 Error	0.0685 ± 0.0098	0.0566 ± 0.0076	0.0635 ± 0.0064	0.0642 ± 0.0080
	Correlation	0.9914 ± 0.0036	0.9937 ± 0.0033	0.9922 ± 0.0036	0.9919 ± 0.0038
	$SSIM$	0.8595 ± 0.0346	0.9059 ± 0.0263	0.8910 ± 0.0263	0.9173 ± 0.0151
B_1 map	l_1 Error	0.0500 ± 0.0210	0.0588 ± 0.0253	0.0723 ± 0.0302	0.0561 ± 0.0273
	Correlation	0.9954 ± 0.0040	0.9947 ± 0.0036	0.9917 ± 0.0044	0.9956 ± 0.0038
	$SSIM$	0.9979 ± 0.0013	0.9974 ± 0.0017	0.9962 ± 0.0028	0.9976 ± 0.0020

Table 1. The quantitative results for T_1 , ρ , and B_1 mapping of the knee on a pixel basis (mean \pm std)

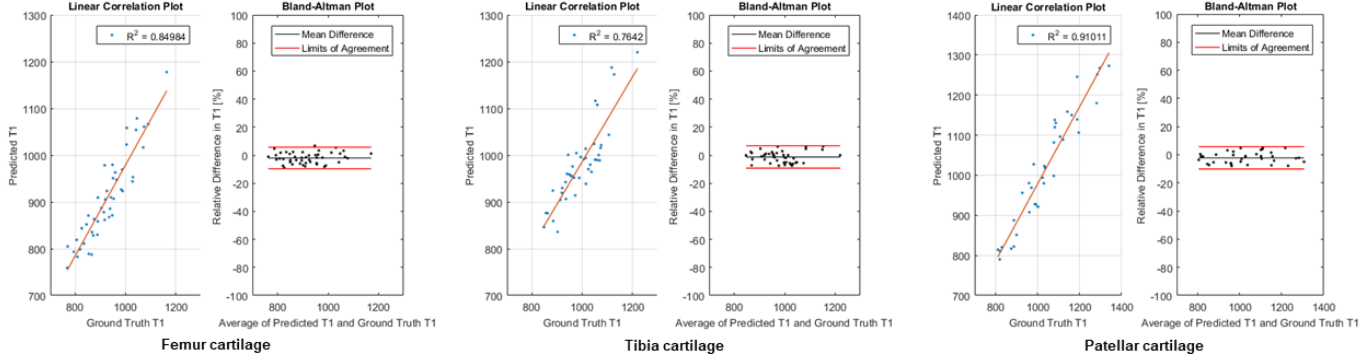


Figure 4. The Bland-Altman plots for T_1 , where every dot corresponds to the averaged T_1 within an ROI (in femur, tibia, or patella cartilage) per subject.

T_1 maps predicted from single input images closely resembled the maps derived from two T_1 -weighted images. In Fig. 5, T_1 maps derived from one image acquired with a flip angle of 20° or 30° were highly similar to the map predicted from both images. On the pixel level, correlation coefficients were 0.9778, 0.9786, and 0.9836 when input images were acquired using a flip angle of 20°, 30°, or both, and l_1 errors were 0.0952, 0.0937, and 0.0567, respectively.

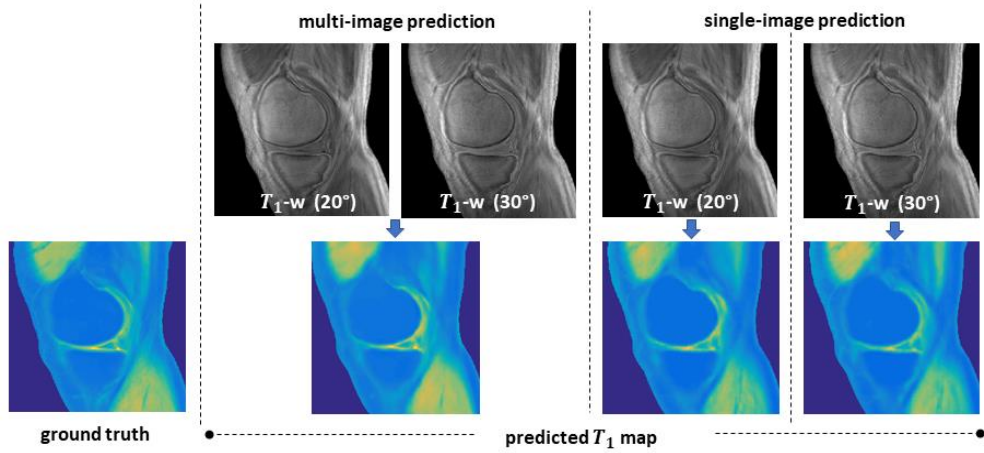


Figure 5. Comparison of T_1 maps of the knee predicted from single input images (acquired using a flip angle of 20° or 30°) with T_1 map derived from both input images. The single input predictions are highly consistent with the dual-input prediction.

It is remarkable that T_1 maps were accurately predicted from a single input image. We believe that the underlying reason for these results is that deep learning takes advantage of the correlation between various quantitative maps and integrates this information into the parametric mapping models as *a priori* knowledge. To validate this argument, we trained deep neural networks to predict T_1 map from ρ map and vice versa. An example is shown in Fig. 6. In the mapping from ρ map to T_1 map, the correlation coefficient and l_1 error were 0.95 ± 0.03 and 0.09 ± 0.01 , respectively; in the inverse mapping, the correlation coefficient and l_1 error were 0.94 ± 0.02 and 0.13 ± 0.02 . Recovery of a high-resolution ρ map from a T_1 map is more challenging because the ground truth T_1 map was slightly smoothed during measurement. This experiment supports the notion that the deep learning models successfully exploit the high correlation between T_1 and ρ maps, which

is believed to serve as *a priori* knowledge and thus effectively reduce the number of input images required for quantitative parametric mapping.

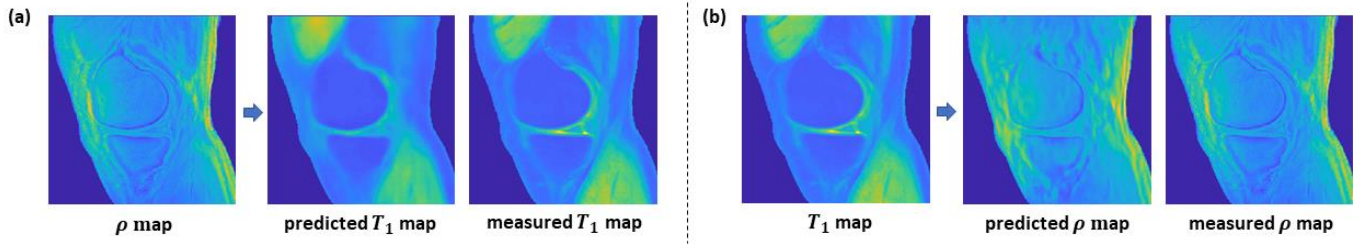


Figure 6. Exploiting the correlation between various tissue parametric maps. (a) T_1 map is predicted from ρ map, confirming that high correlation between the two parametric maps has been deciphered by deep learning. (b) ρ map is predicted from T_1 map. It is more challenging to recover high-resolution ρ map from T_1 map because T_1 map was slightly smoothed during actual measurement. These experiments indicate that high correlation between T_1 map and ρ map has been exploited by deep learning.

T_2^* maps of the knee were predicted from pairs of T_2^* -weighted and T_1 -weighted images. Notice that no additional scan is required because multi-contrast images have already been acquired in standard clinical MRI. Here, the ground truth T_2^* map was measured from six T_2^* -weighted multi-echo images acquired with echo times (TEs) of 0.032, 4.4, 8.8, 13.2, 17.6, and 22 ms, respectively; input images included one of the T_2^* -weighted images (acquired using a specific TE of 4.4, 8.8, 13.2, or 17.6 ms) as well as a T_1 -weighted image (obtained with a flip angle of 20°). A total of 1224 2D images from 59 subjects (including 50 osteoarthritis patients and 9 healthy volunteers) was used for training and testing, with six-fold cross-validation applied.

Excellent agreement was found between the T_2^* maps predicted by deep learning models and the ground truth. A representative case is shown in Fig. 7a. High accuracy was achieved with T_2^* -weighted images predicted using different TEs. The Bland-Altman plots for averaged T_2^* within the femur, tibia, and patella cartilage ROIs are shown in Fig. 7b.

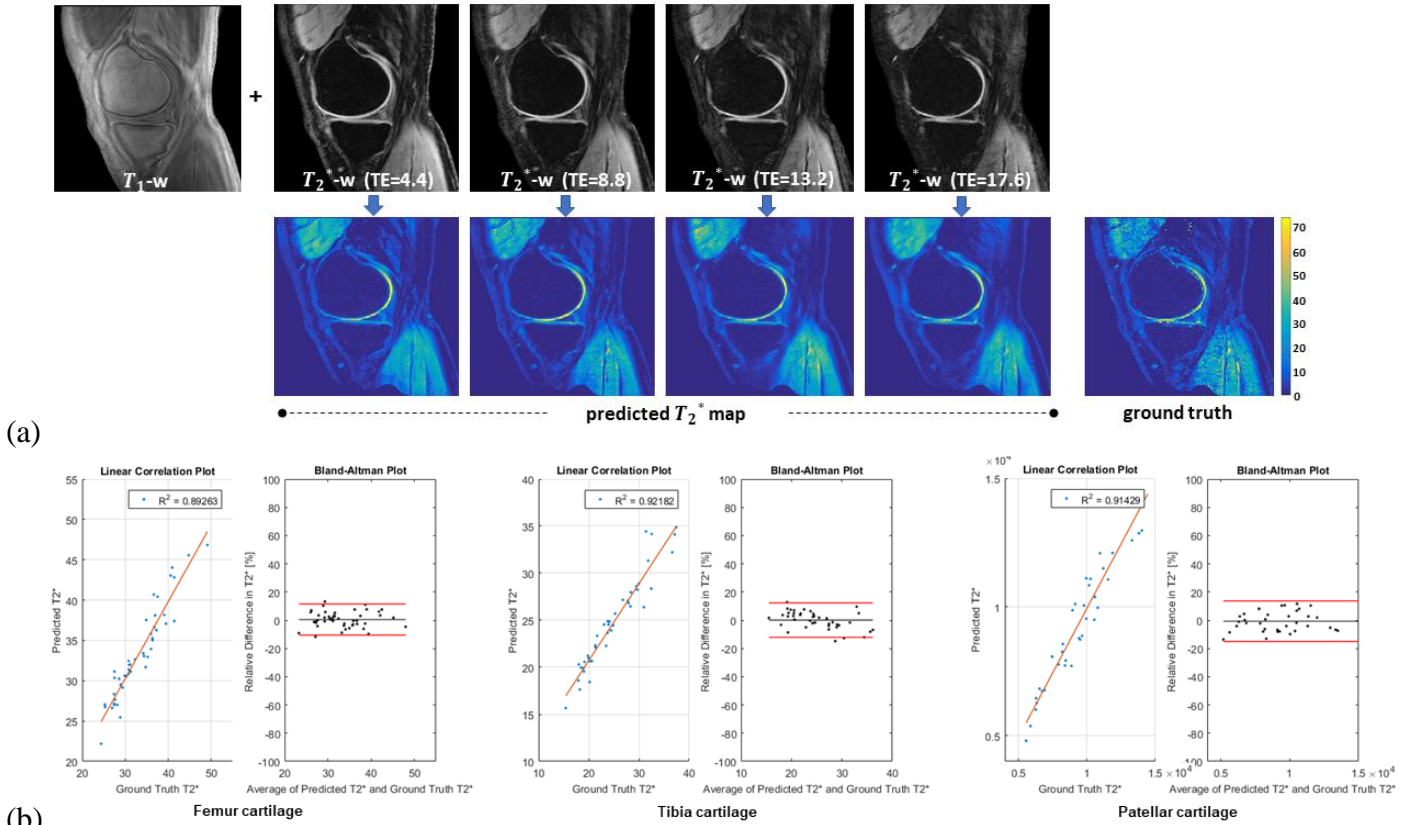
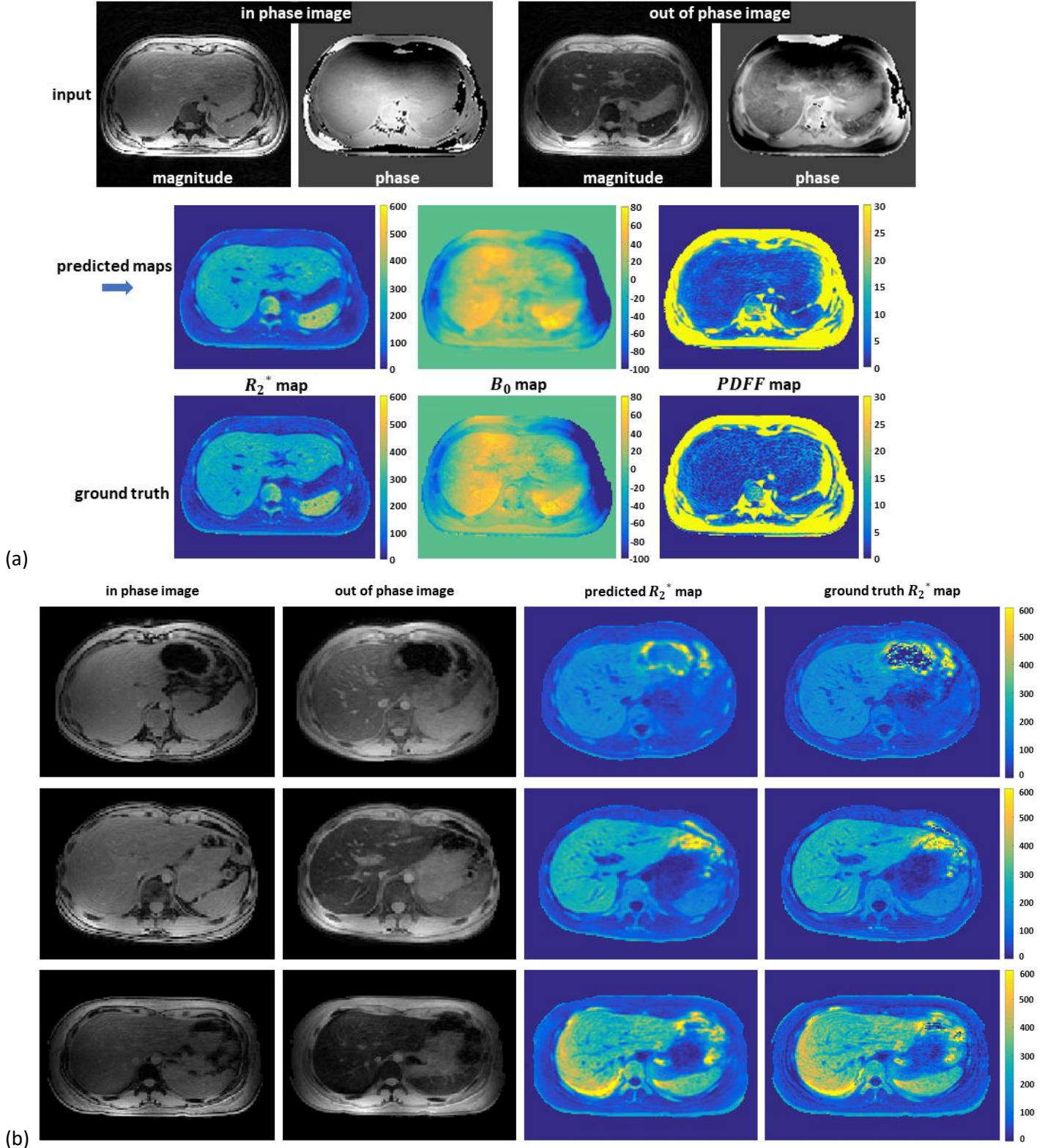


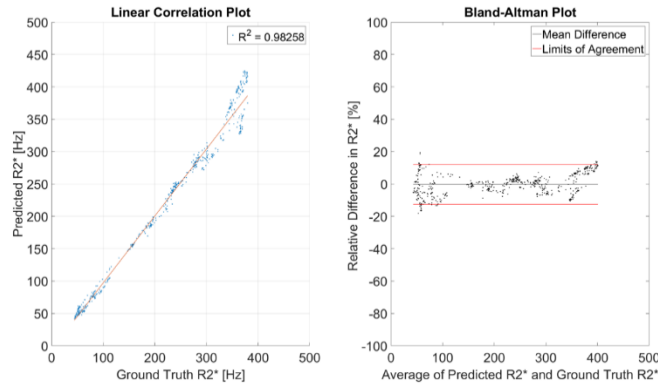
Figure 7. Prediction of T_2^* maps of the knee from T_2^* -weighted images. (a) T_2^* maps are predicted from single T_2^* -weighted images (acquired with a specific TE) and a T_1 -weighted image (obtained using a flip angle of 20°). The T_2^* maps predicted from different input images all have high fidelity to the ground truth maps displayed in the rightmost column. (b) The Bland-Altman plot for T_2^* , where every dot corresponds to averaged T_2^* within an ROI (in femur, tibia, or patella cartilage) for a subject.

R_2^* Mapping of the Liver

In the liver study, R_2^* , B_0 , and $Pdff$ (proton density fat fraction) maps of the liver were predicted from pairs of in-phase and out-of-phase, T_2^* -weighted images. Here, the ground truth R_2^* , B_0 , and $Pdff$ maps were extracted from six multi-echo images using a confounder-corrected model [30]; input images included an in-phase image and an out-of-phase image obtained using a TE of 1.048 ms or 4.084 ms. A total of 1224 2D images (from 26 patients with iron overload) was used for training and testing, where leave-one-out cross-validation was applied.

The resultant maps showed strong correlations to the ground truth. A representative case is shown in Fig. 8a and additional examples of R_2^* maps with various iron overload levels are displayed in Fig. 8b. Within the ROI (i.e., whole liver automatically segmented using the region growing algorithm [31]), the averaged R_2^* was calculated on every slice; the corresponding Bland-Altman plot is shown in Fig. 8c.





(c)

Figure 8. Prediction of R_2^* , B_0 , and $PDFF$ maps of the liver from a pair of in-phase and out-of-phase images. (a) From the magnitude/phase of two T_2^* -weighted images (acquired using TEs of 1.048 ms and 4.084 ms), R_2^* , B_0 , and $PDFF$ maps are predicted (middle row) with high fidelity to the ground truth (bottom row). (b) R_2^* map from three patients with mild, median, and severe iron overload. Each row corresponds to one patient, and high R_2^* values indicate heavy iron overload. The left two columns are input images (magnitude of in-phase/out-of-phase images), while the third and fourth columns represent the predicted and ground truth R_2^* maps, respectively. (c) The Bland-Altman plot for R_2^* , where every dot corresponds to averaged R_2^* within the ROI (i.e., whole liver) in a 2D image.

Methods

We employed self-attention convolutional neural networks to provide end-to-end mapping from a single or very few MR images with conventional T_1/T_2 weighting to the corresponding quantitative parametric maps and field maps. The network has a unique shortcut connection pattern, where relatively dense local shortcuts forward feature maps to all the convolutional blocks in the same hierarchical level, and global shortcuts connect the encoder path and the decoder path [32]. An attention mechanism [33–37] is integrated into the deep neural network to make efficient use of image-wide/non-local information. In every convolutional block, a self-attention layer is combined with the convolutional layer, where the former extracts non-local knowledge (e.g., statistical distribution of tissue relaxation properties) and the latter acquires local information (e.g., smoothness of parametric map or field map) [38]. More details are given in the Appendix (A.3).

The knee images were acquired on two 3T GE MR750 scanners (GE Healthcare Technologies, Milwaukee, WI) with Institutional Review Board (IRB) approval [39, 40]. For every subject, the following images were obtained: four T_1 -weighted images (with a matrix size of $256 \times 256 \times 36$) acquired using flip angles of 5° , 10° , 20° , and 30° ; six T_2^* -weighted images (of the same matrix size) acquired using TEs of 0.032, 4.4, 8.8, 13.2, 17.6, and 22 ms; and a B_1 map (with a matrix size of $128 \times 128 \times 18$) measured using an actual flip angle sequence. Acquisitions for the T_1 -weighted images, T_2^* -weighted images, and B_1 map took 9 min 28 sec, 4 min 57 sec, and 3 min 40 sec, respectively. More details are provided in the Appendix (A.1).

For T_1 mapping of the knee, we trained separate deep neural networks for the prediction of T_1 , ρ , and B_1 maps from a single T_1 -weighted image acquired using a specific flip angle (i.e., 5° , 10° , 20° , or 30°). Notice that we were able to predict the T_1 map without incorporating B_1 map as an input while expecting automatic compensation for B_1 inhomogeneity in the resultant T_1 map.

In T_2^* mapping of the knee, two images with different types of weighting are used as the input because T_2^* decay is a more complicated phenomenon (which could be better described by multi-component model [41]). Using a single T_2^* -weighted image would pose difficulty with TE selection — a long TE leads to signal loss in tissues with ultrashort T_2 relaxation times, but an ultrashort TE is unable to differentiate tissues with long T_2 relaxation times. Incorporating a T_1 -weighted image into the input is a natural choice due to its wide availability in routine MRI examinations.

For T_1 and T_2^* mapping of the knee, a loss function defined as $loss = l_1 + \lambda * (1 - SSIM)$ was employed [42]. Here, l_1 is responsible for minimizing uniform biases, and $SSIM$ (structural similarity index) preserves local structure and high-frequency contrast. λ was empirically chosen as 5. The network parameters were updated using the Adam algorithm [43] with α of 0.001, β_1 of 0.89, β_2 of 0.89, and ϵ of 10^{-8} .

In the liver study, we retrospectively collected free-breathing abdominal MR images acquired on three 3T GE MR750 scanners with IRB approval [44]. For every subject, six T_2^* -weighted images were acquired using a multi-echo sequence with TEs of 0.036, 1.048, 2.060, 3.072, 4.084, and 5.096 ms, respectively. The in-plane resolution was 180×180 , and the slice number per subject varied from 32 to 90 (leading to a scan time between 2 min 54 sec and 6 min 30 sec).

In R_2^* mapping of the liver, we trained deep neural network models to predict R_2^* , B_0 , and $PDFF$ maps from a pair of in-phase and out-of-phase images. Both phase and magnitude images were used for B_0 mapping and $PDFF$ mapping, and magnitude image was employed for R_2^* mapping. In training, l_1 loss was adopted for R_2^* and B_0 mapping, and the mixed l_1 - l_{SSIM} loss was used for $PDFF$ mapping.

Discussion and Conclusions

Derivation of quantitative tissue relaxation properties from standard MR imaging is known to be an ill-posed problem because of the highly complex nature of proton processing and its subtle dependence on not only the molecular structures themselves but also the surrounding microscopic and macroscopic environments. To understand the problem comprehensively and accurately derive mapping information, MRI signal equations corresponding to several parameters need to be solved. Previously, multiple measurements taken using the same pulse sequence have been performed for T_1/T_2 mapping. In Q^2MRI , images acquired using different pulse sequences are used to separate the influence of numerous contributing factors. Using the relationship between quantitative parametric maps and input images learned in training, the deep learning models can predict tissue parametric maps from a single or very few MR images with conventional T_1/T_2 weighting. Therefore, Q^2MRI has potential to transform standard clinical MRI from qualitative imaging to quantitative imaging. Because Q^2MRI is a data-driven method, its accuracy is not degraded by simplified or inaccurate model assumptions in the way that model-based methods are.

The superior capability of the proposed strategy is attributed to the powerful abilities of deep learning to integrate a variety of prior information into one comprehensive parametric mapping model. In conventional approaches, combining *a priori* knowledge is rather difficult. For example, estimating B_1 map from multi-contrast images was accomplished based on a physical model [7, 8, 18, 19] or a statistical model that assumed the distribution of T_1 in different tissues [45, 46] or a linear relationship between $1/\rho$ and $1/T_1$ in brain tissue [47]. However, there was no model that combined *a priori* knowledge in both aspects. On the contrary, deep learning learns different types of *a priori* knowledge and incorporates them into a single model, making it possible to predict the B_1 map from a single T_1 -weighted image with high accuracy.

The deep learning-based modeling provides a way to exploit and utilize the interdependency between various parametric maps. According to quantum statistics [48], various tissue relaxation properties are related (Appendix A.6); and the joint distribution of these random variables is clustered [49]. While Q^2MRI implicitly exploits this interdependency, additional spatial constraint is posed -- the influence of relevant voxels is taken into consideration, via the attention mechanism, for the quantification of tissue parameter at a certain voxel. This improves the robustness of prediction compared to voxel-based parameter fitting approaches. With the incorporation of physical, statistical, and spatial information, the interdependency between various parametric maps and images (e.g., T_1 map and ρ map, B_1 map and T_1 -weighted image) are deciphered and automatically encoded into the parametric mapping models, resulting in significantly reduced need for input data.

Using Q^2MRI , a variety of tissue properties can be predicted from very few images with conventional T_1/T_2 weighting. First, derivation of quantitative parametric maps from MR images without the corresponding weighting is possible (e.g., predicting $T_{1\rho}$ map from conventional MR images without $T_{1\rho}$ weighting). When the physical, statistical, and spatial relationships between T_1 , T_2 , and $T_{1\rho}$ are exploited, the $T_{1\rho}$ map can be estimated from T_1 and T_2 maps (which is similar to the prediction of T_1 map from ρ map). Since T_1 and T_2 maps are predictable from few MR images with conventional T_1/T_2 weighting (as demonstrated in the study), $T_{1\rho}$ map is likely to be derived from the same input images without $T_{1\rho}$ weighting. This has been partially validated in a previous study, where a $T_{1\rho}$ -weighted image was accurately predicted from the combination of a T_1 -weighted image and a T_2^* -weighted image [50]. More generally, a variety of biophysical and biochemical parametric maps can be derived using the same strategy, where the influences of contributive factors are separated from input images and combined in a way that mimics the physical model used to extract the ground truth map. For example, in $PDFF$ mapping, T_1 -related bias, T_2^* decay, and spectral complexity of fat are believed to be implicitly extracted and used to form the confounder model (which combines least squares fitting of complex-valued source images with multi-peak fat modeling [30]).

Q^2MRI is a general quantitative parametric mapping framework. The input images can be acquired using a flexible imaging protocol. For instance, T_1 map can be predicted from a T_1 -weighted image acquired using a flexible flip angle. Similarly, when a slightly different imaging protocol is used to provide input images with T_1 and T_2^* weighting, the parametric mapping models can simply be updated with transfer learning [51]. A scanner-independent model can be trained with data acquired from a collection of MRI scanners, as demonstrated in our study. The quantitative parametric mapping strategy is not confined to the proposed deep learning technique. Alternative network architectures could be

employed for this task, and with the rapid advancements in artificial intelligence, further performance improvements and functionality enhancements can be expected.

Q^2MRI also provides an opportunity to take full advantage of the versatility of MRI contrast. While MRI can offer versatile soft tissue contrasts to meet different clinical demands, this unique feature of MRI has never been fully utilized in practice because of the significant data acquisition overhead associated with each change of acquisition parameters. The proposed parametric mapping framework presents a simple solution that fits into a routine MRI examination workflow: after tissue properties have been estimated using Q^2MRI , MRI contrast can be retrospectively tuned with the application of Bloch equations. An example of changing contrast in T_1 -weighted images (with alternative flip angles) is demonstrated in the Appendix (A.4). With the application of various pulse sequences on multi-parametric maps, a wide spectrum of image contrasts can be retrospectively obtained. In fact, Q^2MRI also provides theoretical support to MRI contrast translation (i.e., direct mapping from one image contrast to another without the involvement of quantitative parametric maps). For example, predicting contrast-enhanced MRI from non-contrast enhanced images can be reframed as multi-step processing that includes estimating the T_1 map, changing the T_1 value of blood, then formulating the contrast-enhanced image based on the modified T_1 map. With the feasibility of parametric mapping now confirmed by Q^2MRI , deep learning-based MRI contrast translation has been conceptually substantiated [52, 53].

In summary, a new paradigm of data-driven Q^2MRI strategy is presented for quantitative tissue parametric mapping. A significant practical benefit of Q^2MRI is that no additional scans are required for generating quantitative parametric maps. The extraordinary capability of deep learning in deriving qualitative MR parametric maps from a single or very few MR images with conventional T_1 / T_2 weighting is demonstrated in knee and liver studies. Because Q^2MRI has no requirements with regards to the imaging protocol used for input image acquisition, a variety of quantitative parametric maps can be derived from images that are routinely obtained in clinical practice, facilitating the conduct of quantitative image analysis in prospective and retrospective studies. In radiation therapy, Q^2MRI will aid MRI-only treatment planning [54] and image-guided therapy [55]. With the application of Bloch equations, MR imaging can be tailored to individual patients, with contrasts chosen to meet their specific clinical demands. The proposed Q^2MRI method can be further extended to quantification of other tissue parameters for diverse clinical applications. As healthcare and biomedicine are transforming into digitized and data intensive disciplines, quantitative imaging capabilities enabled by Q^2MRI may find valuable applications in the future and promise to benefit a wide spectrum of biomedical applications.

Acknowledgments: The authors would like to thank Drs. Charles Mistretta, Brian Rutt, Debiao Li, Rohan Dharmakumar, Garry Gold, Zhitao Li, Christopher Sandino, Aiming Lu, Huimin Wu, Jing Liu, Nicole Le, Maria Chan, and Cheng Tang for their helpful discussion.

Funding: This research is partially supported by NIH/NCI (1R01 CA256890, 1R01 CA227713), NIH/NIAMS (1R01 AR068987), and NIH/NINDS (1R01 NS092650), and NIH/NIBIB (1R01 EB026136). The contents of this article are solely the responsibility of the authors and do not necessarily represent the official NIH views.

Author contributions: L.X. proposed the strategy of using deep learning to separate the influence of different contributive factors from single MR images and thus derive quantitative parametric maps from clinical routine without additional acquisition. He guided the direction of the research. Y.W. conducted parametric mapping experiments, hypothesized how deep learning extracts *a priori* information and exploits the interdependency within/across MRI parameter subspaces. Y.M. and J.D. provided knee data and proposed to exclude B_1 map in T_1 mapping. S.V., Y.K., M.A. and J.P. provided liver data and suggested to use complex data for parametric mapping. S.V., E.Y.C. and S.H. evaluated the clinical efficacy. N.K., D. C. and H.R. performed preprocessing. The manuscript was written by Y. W., L.X., S.V. and J.D., and revised by all authors.

Competing interests: L.X. and Y.W. are co-inventors on patents based on this work [66, 67].

Data and materials availability: Source code is available from the corresponding author upon request.

Supplementary Material

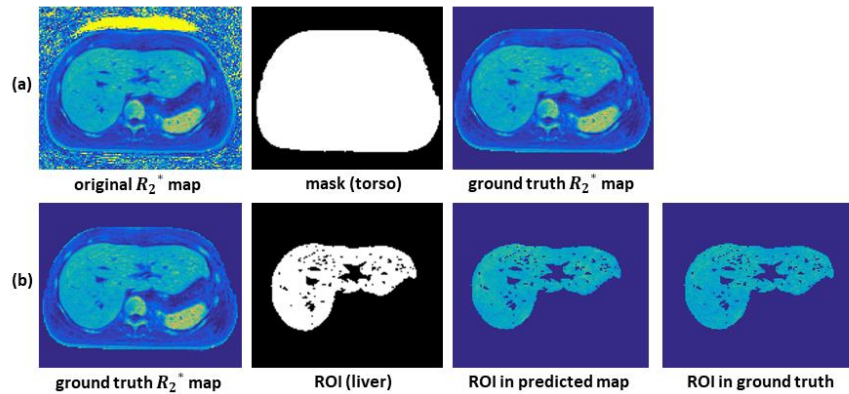
A.1. Image acquisition

In this study, T_1 - and T_2^* -weighted knee images were acquired on 3T GE MR750 scanners [39, 40]. For every subject, the following images were obtained: four T_1 -weighted images acquired using an ultrashort echo time (UTE) cones sequence with flip angles of 5°, 10°, 20°, and 30° respectively, a TE (echo time) of 32 μ s, and a TR (time of repetition) of 20 ms; six T_2^* -weighted images acquired using a multi-echo sequence with TEs of 0.032, 4.4, 8.8, 13.2, 17.6 and 22 ms, a TR of 28 ms, and a flip angle of 16°; and finally a B_1 map measured using an actual flip angle sequence [9] with a TE of 32 μ s, two interleaved TRs (20/100ms), and a flip angle of 45°. Notice that the incorporation of the B_1 map was important for variable-flip angle T_1 mapping (a 20% difference in B_1 map, which is typical at 3T, causes a 44% error in T_1 map). The ground truth T_1 and T_2^* maps were extracted using the Levenberg-Marquardt algorithm [56].

In the liver, free-breathing abdominal MR images were acquired on three 3T GE MR750 scanners [44]. For every subject, six T_2^* -weighted images were acquired using a multi-echo cones sequence with TEs of 0.036, 1.048, 2.060, 3.072, 4.084, and 5.096 ms respectively, a TR of 11ms, and a flip angle of 3°. The ground truth R_2^* , B_0 , and $PDFF$ maps were calculated from six multi-echo images based on the confounder model, which combines least squares fitting of complex-valued source images with multi-peak fat modeling. While cones acquisition is robust to motion, some data acquired in the free-breathing condition was of low image quality and thus excluded. High quality images from 26 patients were used in this study.

A.2. Segmentation

In preprocessing, the torso is first delineated to eliminate background noise from outside the human body. For regional quantitative analysis, the whole liver was segmented using the region growing algorithm (S1). The generated ROI was then applied on predicted and ground truth parametric maps for quantitative analysis.

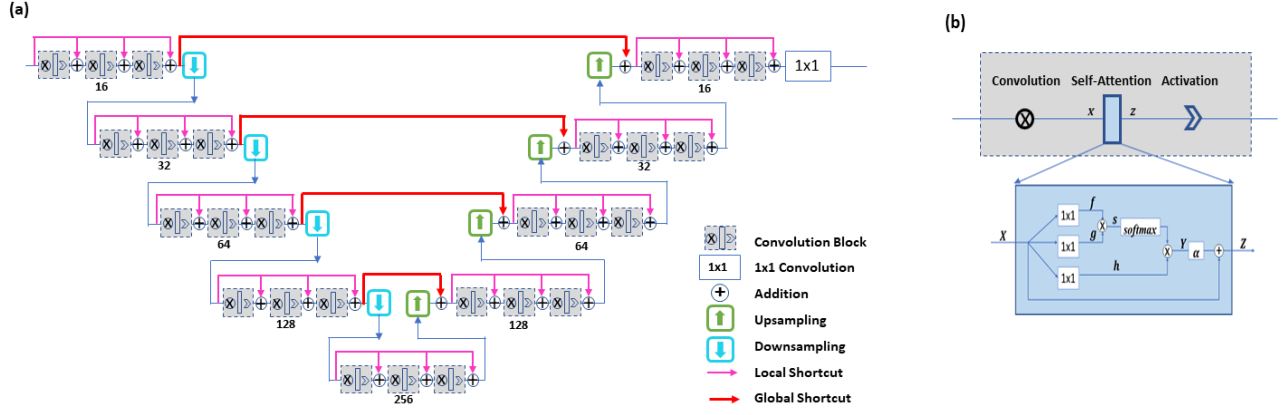


S1. Segmentation as preprocessing. (a) Torso is delineated to prevent background noise from outside the human body. (b) The whole liver is segmented using the region growing algorithm.

A.3. Hyperparameters of deep neural networks

For the proposed parametric mapping tasks, a self-attention convolutional neural network architecture was employed (S2). The network has a unique shortcut connection pattern as inspired by V-net, DenseNet, and other methods [57-61]. Here, relatively dense local shortcuts forward feature maps to all the convolutional blocks in the same hierarchical level, and global shortcuts connect the encoder path and the decoder path, effectively facilitating residual learning [62, 63].

In the hierarchical network, features are extracted at various scales. At each level, there are three convolutional blocks. Every convolutional block is composed of a convolutional layer, a self-attention layer, and a nonlinear activation layer. At the convolutional layer, image features are extracted using 3×3 convolutional kernels. At the self-attention layer, the self-attention maps are derived for feature maps extracted at the preceding convolutional layer. At the activation layer, the Parametric Rectified Linear Unit (PReLU) function is applied. Down-sampling and up-sampling are accomplished using 2×2 convolutional kernels with a stride of 2 [59]. In the knee studies, every network had five hierarchical levels (with 16, 32, 64, 128, and 256 channels in every level, respectively). In the liver study, the networks for R_2^* mapping and B_0 mapping had three hierarchical levels (with 16, 32, and 64 channels in every level, respectively), whereas the network for $PDFF$ mapping had five hierarchical levels (with 16, 32, 64, 128, and 256 channels in every level, respectively).



S2. The proposed self-attention convolutional neural network. (a) A hierarchical network with global shortcuts and densely connected local shortcuts. (b) A convolutional block with a self-attention layer integrated. X is the input (preceding feature map), Y is the attention map, and Z is the output of the convolutional block. The attention map Y is determined by s (relevance between the given pixel and the other pixel) and h (feature representation of the other pixel). In the output Z , the contributions from local information (feature map X) and non-local information (attention map Y) are balanced by a scalar α .

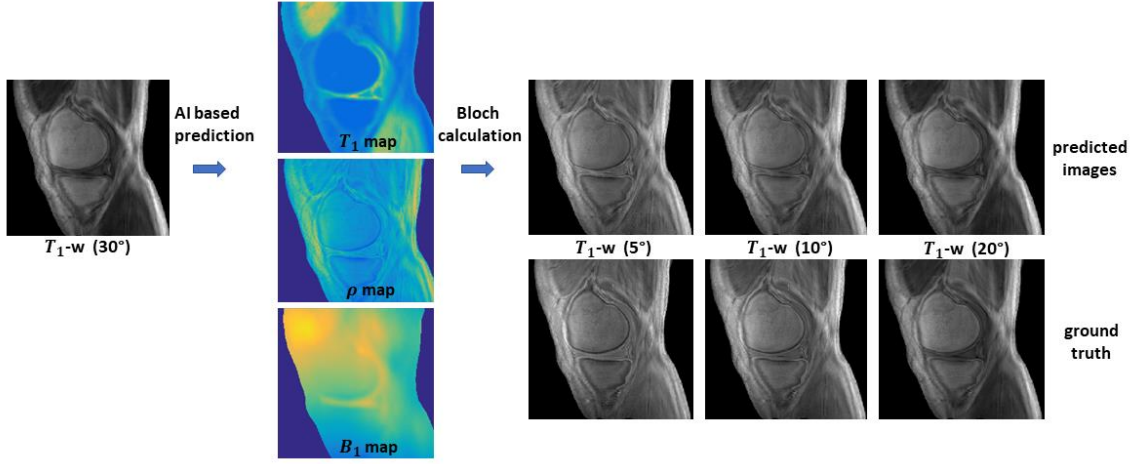
Motivated by [33-37], the attention mechanism has been integrated into the deep neural network to exploit image-wide/non-local *a priori* information with higher efficiency. In conventional deep neural networks, long-range dependency (i.e., interaction between widely separated pixels) is progressively propagated across multiple layers, which may cause optimization difficulties. A self-attention network, on the other hand, overcomes this limitation by establishing direct interactions between a given pixel and all the other pixels in the feature map. The intensity of a direct interaction is determined by two factors: relevance between the given pixel and the other pixel, and features of the other pixel. We quantify the relevance between the two pixels using an embedded Gaussian function $s(X_i, X_j) = \exp\{(W_f X_i)'(W_g X_j)\}$, and represent the feature of the other pixel with a linear function $h(X_j) = W_h X_j$, where W_f , W_g , and W_h are weight matrices learned in training. Unlike a transformer [36], the proposed network combines a self-attention module with the convolutional layer, where the former extracts non-local knowledge and the latter acquires local information. The attention mechanism is more influential when the receptive field of the network is small. In the liver study (where the network had fewer hierarchical levels), R_2^* mapping could not be accomplished without self-attention.

In the loss function $loss = l_1 + \lambda * (1 - SSIM)$, $SSIM$ is defined as $SSIM(x, y) = \frac{(2\mu_x\mu_y + C_1)(2\sigma_x\sigma_y + C_2)}{(\mu_x^2 + \mu_y^2 + C_1)(\sigma_x^2 + \sigma_y^2 + C_2)}$, where μ_x , μ_y , σ_x , and σ_y correspond to the mean and standard deviation of signal intensity in the reconstructed image x and the ground truth y , and C_1 and C_2 are constants [42]. Comparison of the mixed $l_1 - l_{SSIM}$ loss with l_1 loss has been performed previously in [26]. To evaluate prediction accuracy, correlation coefficient was used, defined as $orr(x, y) = \frac{2\sigma_{xy}}{\sigma_x^2 + \sigma_y^2 + (\mu_x - \mu_y)^2}$.

The network was implemented on a TensorFlow-based AI platform NiftyNet [64, 65]. Computations were performed on a desktop computer running Linux operating system with an Intel i77700K CPU (4.2 GHz, and 32GB memory) and Nvidia GPU GeForce GTX1070.

A.4. Retrospective contrast tuning

After quantitative parametric maps are estimated using Q^2MRI , MRI contrast can be retrospectively tuned with the application of Bloch equations. As an example, we derived variable-flip-angle images from a single T_1 -weighted image. Based on the T_1 , ρ and B_1 maps predicted from a T_1 -weighted image (acquired using a flip angle of 30°), other T_1 -weighted images were obtained according to $S = \rho \cdot \sin(\alpha) \frac{1 - e^{-TR/T_1}}{1 - \cos(\alpha) \cdot e^{-TR/T_1}}$. Here, B_1 inhomogeneity is taken into consideration via $\alpha = \alpha_{nominal} \cdot B_1$, where $\alpha_{nominal}$ is the nominal flip angle specified by the imaging protocol and α is the actual flip angle that takes effects. The predicted images (corresponding to flip angles of 5° , 10° , and 20° , respectively) were compared with the ground truth, and high fidelity was achieved (S3, Table 2). More tissue contrasts can be obtained by taking other values of imaging parameters (flip angle, TR).



S3. Retrospective tuning of tissue contrast in T_1 -weighted image. Given a single T_1 -weighted image (acquired using a flip angle of 30°), T_1 , ρ and B_1 maps are predicted and used to synthesize images (corresponding to flip angles of 5°, 10°, and 20°). High fidelity is achieved in the resultant images.

Correlation					l_1 Error				
input \ target	T_1 w (5°)	T_1 w (10°)	T_1 w (20°)	T_1 w (30°)	input \ target	T_1 w (5°)	T_1 w (10°)	T_1 w (20°)	T_1 w (30°)
T_1 w (5°)	0.9880 ± 0.0044	0.9774 ± 0.0061	0.9849 ± 0.0040	0.9762 ± 0.0072	T_1 w (5°)	0.0585 ± 0.0111	0.0793 ± 0.0137	0.0693 ± 0.0156	0.0892 ± 0.0216
T_1 w (10°)	0.9817 ± 0.0054	0.9933 ± 0.0018	0.9915 ± 0.0009	0.9845 ± 0.0034	T_1 w (10°)	0.0716 ± 0.0130	0.0441 ± 0.0069	0.0537 ± 0.0085	0.0730 ± 0.0152
T_1 w (20°)	0.9754 ± 0.0086	0.9888 ± 0.0030	0.9950 ± 0.0009	0.9893 ± 0.0028	T_1 w (20°)	0.0819 ± 0.0171	0.0570 ± 0.0093	0.0426 ± 0.0065	0.0617 ± 0.0120
T_1 w (30°)	0.9702 ± 0.0104	0.9853 ± 0.0051	0.9929 ± 0.0009	0.9912 ± 0.0021	T_1 w (30°)	0.0897 ± 0.0198	0.0661 ± 0.0129	0.0504 ± 0.0083	0.0543 ± 0.0116

		Predicting images from a T_1 w image				Predicting images from T_1 w and T_2 w images			
	Output Input	T_1 w (5°)	T_1 w (10°)	T_1 w (20°)	T_1 w (30°)	T_1 w (5°)	T_1 w (10°)	T_1 w (20°)	T_1 w (30°)
l_1 Error	5°	0.0559 ± 0.0104	0.0706 ± 0.0063	0.1177 ± 0.0174	0.1472 ± 0.0212	0.0719 ± 0.0118	0.0688 ± 0.0087	0.0923 ± 0.0130	0.1159 ± 0.0144
	10°	0.0777 ± 0.0141	0.0456 ± 0.0046	0.0918 ± 0.0145	0.1256 ± 0.0213	0.0714 ± 0.0140	0.0368 ± 0.0048	0.0760 ± 0.0096	0.1071 ± 0.0136
	20°	0.1040 ± 0.0114	0.0765 ± 0.0067	0.0743 ± 0.0184	0.1093 ± 0.0250	0.0826 ± 0.0115	0.0570 ± 0.0064	0.0679 ± 0.0165	0.1044 ± 0.0244
	30°	0.1106 ± 0.0111	0.0900 ± 0.0090	0.0843 ± 0.0133	0.0916 ± 0.0198	0.0830 ± 0.0111	0.0646 ± 0.0078	0.0733 ± 0.0100	0.0887 ± 0.0177
SSIM	5°	0.9909 ± 0.0017	0.8894 ± 0.0288	0.8217 ± 0.0341	0.7812 ± 0.0363	0.9540 ± 0.0057	0.8879 ± 0.0293	0.8433 ± 0.0357	0.8135 ± 0.0381
	10°	0.8897 ± 0.0279	0.9849 ± 0.0029	0.8930 ± 0.0212	0.8525 ± 0.0247	0.8985 ± 0.0278	0.9930 ± 0.0024	0.9089 ± 0.0224	0.8743 ± 0.0250
	20°	0.8220 ± 0.0348	0.8910 ± 0.0230	0.9666 ± 0.0077	0.9026 ± 0.0120	0.8681 ± 0.0331	0.9194 ± 0.0221	0.9646 ± 0.0083	0.9018 ± 0.0136
	30°	0.7812 ± 0.0373	0.8501 ± 0.0270	0.9071 ± 0.0111	0.9596 ± 0.0085	0.8497 ± 0.0356	0.8969 ± 0.0251	0.9127 ± 0.0111	0.9412 ± 0.0076
Correlation Coefficient	5°	0.9977 ± 0.0008	0.9919 ± 0.0027	0.9796 ± 0.0073	0.9718 ± 0.0103	0.9961 ± 0.0013	0.9940 ± 0.0024	0.9889 ± 0.0039	0.9843 ± 0.0055
	10°	0.9918 ± 0.0026	0.9969 ± 0.0011	0.9890 ± 0.0035	0.9822 ± 0.0058	0.9939 ± 0.0021	0.9983 ± 0.0008	0.9929 ± 0.0024	0.9877 ± 0.0043
	20°	0.9821 ± 0.0049	0.9906 ± 0.0028	0.9929 ± 0.0034	0.9873 ± 0.0051	0.9900 ± 0.0033	0.9949 ± 0.0018	0.9949 ± 0.0017	0.9895 ± 0.0029
	30°	0.9786 ± 0.0060	0.9870 ± 0.0038	0.9909 ± 0.0033	0.9899 ± 0.0044	0.9888 ± 0.0037	0.9932 ± 0.0024	0.9933 ± 0.0020	0.9914 ± 0.0033

Table 2. Evaluation of variable contrast image predictions. In each row, images with a certain contrast (presumably acquired using a specific flip angle) are predicted from different input images. Both low l_1 errors (between 0.04 and 0.09) and high correlation coefficients (ranging from 0.97 to 0.99) are consistently achieved on a pixel basis when different flip angles are used for input and output images.

A.5. Interdependency between various relaxation parametric maps

In quantum statistics [48], T_1 , T_2 , and ρ are related by the following:

$$\frac{1}{T_1} = \frac{3}{10} b^2 [J(\omega_0) + 4J(2\omega_0)] \text{ and } \frac{1}{T_2} = \frac{3}{20} b^2 [3J(0) + 5J(\omega_0) + 2J(2\omega_0)],$$

where $J(\omega_0)$ is the spectral density function at the resonance frequency expressed by:

$$J(\omega_0) = \int_{-\infty}^{\infty} G(\tau) \exp(-i\omega_0\tau) d\tau. \quad b = -\frac{h\gamma^2}{r^3}.$$

In Q^2MRI , this complicated relationship between various tissue relaxation properties is exploited and encoded into a parametric mapping model as *a priori* knowledge. Along with other spatial and statistical information, the correlation between various parametric maps is deciphered.

Integrating the correlation between various parametric maps into quantitative parametric mapping model enables the derivation of T_1 map from a single T_1 -weighted image. In a T_1 -weighted image, the signal intensity is a function of both T_1 and ρ , $S = f_1(T_1, \rho)$. If ρ can be represented as a function of T_1 (i.e., $\rho = m(T_1)$), then the signal intensity is a function of T_1 (i.e., $S = f_2(T_1)$). The inverse problem of deriving T_1 from a single T_1 -weighted image is no longer an ill-posed problem.

A.6. Exploiting *a priori* information in high-dimensional MRI parameter space

In Q^2MRI , *a priori* information is exploited not only within the tissue property subspace (A.5), but also across different subspaces. For instance, a subtle connection between the tissue property subspace and the system condition subspace is established when the interdependency between B_1 and MR signals are exploited.

It is established that there is a relationship between B_1 and MR signal caused by the electrodynamic interaction between the incident transmission radiofrequency field and human anatomy [20]. In Q^2MRI , this relationship is exploited as *a priori* knowledge and encoded into parametric mapping models.

Moreover, in Q^2MRI , spatial and statistical knowledge is seamlessly incorporated. In previous approaches, similar information (e.g., the statistical distribution of T_1 in different tissues [54, 55] or the linear relationship between $1/\rho$ and $1/T_1$ in brain tissue [56]) were used to estimate the B_1 map from multiple input images, but it was difficult to combine them with each other or with physical models. In Q^2MRI , with seamless incorporation of *a priori* information relevant to different aspects, the B_1 map is estimated from only a single input image.

The implicit integration of the predicted B_1 map into the T_1 mapping model helps compensate for B_1 inhomogeneity without the need to perform actual measurement of the B_1 map. In a T_1 -weighted image, the signal intensity is a function of T_1 , ρ , and B_1 ($S = f_3(T_1, \rho, B_1)$). If B_1 can be represented as a function of the signal intensity ($B_1 = n(S)$) and $\rho = m(T_1)$, then the T_1 map can be derived from a single T_1 -weighted image with B_1 compensation being automatically achieved ($T_1 = f_4(S)$). Here, the acquisition parameter subspace and the system condition subspace are connected ($\alpha = \alpha_{nominal} \cdot B_1$).

References

- [1] Liang ZP, Lauterbur PC. Principles of magnetic resonance imaging: a signal processing perspective. *SPIE Optical Engineering Press*; 2000.
- [2] Li R, Xing L, Napel S, Rubin DL, editors. Radiomics and radiogenomics: technical basis and clinical applications. CRC Press; 2019 Jul 9.
- [3] H. Z. Wang, S. J. Riederer, and J. N. Lee, "Optimizing the precision in T1 relaxation estimation using limited flip angles," *Magnetic Resonance in Medicine*, vol. 5, pp. 399-416, 1987.
- [4] Chavhan GB, Babyn PS, Thomas B, Shroff MM, Haacke EM. Principles, techniques, and applications of T2*-based MR imaging and its special applications. *Radiographics*. 2009 Sep;29(5):1433-49.
- [5] S. C. Deoni, T. M. Peters, and B. K. Rutt, "High-resolution T1 and T2 mapping of the brain in a clinically acceptable time with DESPOT1 and DESPOT2," *Magnetic Resonance in Medicine*, vol. 53, pp. 237-241, 2005.
- [6] Duvvuri U, Reddy R, Patel SD, Kaufman JH, Kneeland JB, Leigh JS. T1p-relaxation in articular cartilage: effects of enzymatic degradation. *Magnetic resonance in medicine*. 1997 Dec;38(6):863-7.
- [7] S. C. Deoni, "High-resolution T1 mapping of the brain at 3T with driven equilibrium single pulse observation of T1 with high-speed incorporation of RF field inhomogeneities (DESPOT1-HIFI)," *Journal of Magnetic Resonance Imaging*, vol. 26, pp. 1106-1111, 2007.
- [8] Robinson S, Jovicich J. B0 mapping with multi-channel RF coils at high field. *Magnetic resonance in medicine*, 2011 Oct;66(4):976-88.
- [9] V. L. Yarnykh, "Actual flip-angle imaging in the pulsed steady state: a method for rapid three-dimensional mapping of the transmitted radiofrequency field," *Magnetic Resonance in Medicine*, vol. 57, pp. 192-200, 2007.
- [10] R. Treier, A. Steingoetter, M. Fried, W. Schwizer, and P. Boesiger, "Optimized and combined T1 and B1 mapping technique for fast and accurate T1 quantification in contrast-enhanced abdominal MRI," *Magnetic Resonance in Medicine*, vol. 57, pp. 568-576, 2007.
- [11] Lustig M, Donoho DL, Santos JM, Pauly JM. Compressed sensing MRI. *IEEE signal processing magazine*. 2008 Mar 21;25(2):72-82.
- [12] Doneva M, Börnert P, Eggers H, Stehning C, S  n  gas J, Mertins A. Compressed sensing reconstruction for magnetic resonance parameter mapping. *Magnetic Resonance in Medicine*, 2010 Oct;64(4):1114-20.
- [13] Velikina JV, Alexander AL, Samsonov A. Accelerating MR parameter mapping using sparsity-promoting regularization in parametric dimension. *Magnetic resonance in medicine*, 2013 Nov;70(5):1263-73.
- [14] Zhao B, Lu W, Hitchens TK, Lam F, Ho C, Liang ZP. Accelerated MR parameter mapping with low-rank and sparsity constraints. *Magnetic resonance in medicine*, 2015 Aug;74(2):489-98.

- [15] P. Schmitt, M. A. Griswold, P. M. Jakob, M. Kotas, V. Gulani, M. Flentje, *et al.*, "Inversion recovery TrueFISP: quantification of T1, T2, and spin density," *Magnetic Resonance in Medicine*, vol. 51, pp. 661-667, 2004
- [16] Ma D, Gulani V, Seiberlich N, Liu K, Sunshine JL, Duerk JL, Griswold MA. Magnetic resonance fingerprinting. *Nature*. 2013 Mar;495(7440):187-92.
- [17] Davies M, Puy G, Vandergheynst P, Wiaux Y. A compressed sensing framework for magnetic resonance fingerprinting. *Siam journal on imaging sciences*. 2014;7(4):2623-56.
- [18] Cloos MA, Knoll F, Zhao T, Block KT, Bruno M, Wiggins GC, Sodickson DK. Multiparametric imaging with heterogeneous radiofrequency fields. *Nature communications*. 2016 Aug 16;7(1):1-0.
- [19] G. Körzdörfer, Y. Jiang, P. Speier, J. Pang, D. Ma, J. Pfeuffer, *et al.*, "Magnetic resonance field fingerprinting," *Magnetic resonance in medicine*, vol. 81, pp. 2347-2359, 2019.
- [20] Wyatt CR, Barbara TM, Guimaraes AR. T1p magnetic resonance fingerprinting. *NMR in Biomedicine*. 2020 May;33(5):e4284.
- [21] Tanenbaum LN, Tsiouris AJ, Johnson AN, Naidich TP, DeLano MC, Melhem ER, Quarterman P, Parameswaran SX, Shankaranarayanan A, Goyen M, Field AS. Synthetic MRI for clinical neuroimaging: results of the Magnetic Resonance Image Compilation (MAGiC) prospective, multicenter, multireader trial. *American Journal of Neuroradiology*. 2017 Jun 1;38(6):1103-10.
- [22] Christodoulou AG, Shaw JL, Nguyen C, Yang Q, Xie Y, Wang N, Li D. Magnetic resonance multitasking for motion-resolved quantitative cardiovascular imaging. *Nature biomedical engineering*. 2018 Apr;2(4):215-26.
- [23] Wang F, Dong Z, Reese TG, Bilgic B, Katherine Manhard M, Chen J, Polimeni JR, Wald LL, Setsompop K. Echo planar time-resolved imaging (EPTI). *Magnetic resonance in medicine*. 2019 Jun;81(6):3599-615.
- [24] Y. LeCun, Y. Bengio, and G. Hinton, "Deep learning," *nature*, vol. 521, p. 436, 2015.
- [25] Cohen O, Zhu B, Rosen MS. MR fingerprinting deep reconstruction network (DRONE). *Magnetic resonance in medicine*. 2018 Sep;80(3):885-94.
- [26] Wu Y, Ma Y, Du J, Xing L. Accelerating quantitative MR imaging with the incorporation of B1 compensation using deep learning. *Magnetic Resonance Imaging*. 2020 Oct 1;72:78-86.[8].
- [27] Xing, Lei, Maryellen L. Giger, and James K. Min, eds. *Artificial intelligence in medicine: technical basis and clinical applications*. Academic Press, 2020.
- [28] Wang Y, Liu T. Quantitative susceptibility mapping (QSM): decoding MRI data for a tissue magnetic biomarker. *Magnetic resonance in medicine*, 2015 Jan;73(1):82-101.
- [29] Reeder SB, Hu HH, Sirlin CB. Proton density fat-fraction: a standardized MR-based biomarker of tissue fat concentration. *Journal of magnetic resonance imaging*, 2012 Nov;36(5):1011.
- [30] Hernando D, Kellman P, Haldar JP, Liang ZP. Robust water/fat separation in the presence of large field inhomogeneities using a graph cut algorithm. *Magnetic Resonance in Medicine*. 2010 Jan;63(1):79-90.
- [31] Hojjatoleslami SA, Kittler J. Region growing: a new approach. *IEEE Transactions on Image processing*. 1998 Jul;7(7):1079-84.
- [32] Y. Wu, Y. Ma, D. P. Capaldi, J. Liu, W. Zhao, J. Du, *et al.*, "Incorporating prior knowledge via volumetric deep residual network to optimize the reconstruction of sparsely sampled MRI," *Magnetic resonance imaging*, 2019.
- [33] S. Hochreiter and J. Schmidhuber, "Long short-term memory," *Neural computation*, vol. 9, pp. 1735-1780, 1997.
- [34] M.-T. Luong, H. Pham, and C. D. Manning, "Effective approaches to attention-based neural machine translation," *arXiv preprint arXiv:1508.04025*, 2015.
- [35] X. Wang, R. Girshick, A. Gupta, and K. He, "Non-local neural networks," in *Proceedings of the IEEE Conference on Computer Vision and Pattern Recognition*, 2018, pp. 7794-7803.
- [36] A. Vaswani, N. Shazeer, N. Parmar, J. Uszkoreit, L. Jones, A. N. Gomez, *et al.*, "Attention is all you need," in *Advances in Neural Information Processing Systems*, 2017, pp. 5998-6008.
- [37] H. Zhang, I. Goodfellow, D. Metaxas, and A. Odena, "Self-attention generative adversarial networks," *arXiv preprint arXiv:1805.08318*, 2018.
- [38] Y. Wu, Y. Ma, J. Liu, J. Du, and L. Xing, "Self-attention convolutional neural network for improved MR image reconstruction," *Information Sciences*, vol. 490, pp. 317-328, 2019.
- [39] Du, Jiang, *et al.* "Qualitative and quantitative ultrashort echo time (UTE) imaging of cortical bone." *Journal of Magnetic Resonance* 207.2 (2010): 304-311.
- [40] Y. J. Ma, W. Zhao, L. Wan, T. Guo, A. Searleman, H. Jang, *et al.*, "Whole knee joint T1 values measured in vivo at 3T by combined 3D ultrashort echo time cones actual flip angle and variable flip angle methods," *Magnetic resonance in medicine*, vol. 81, pp. 1634-1644, 2019.

- [41] J. Du, E. Diaz, M. Carl, W. Bae, C. B. Chung, and G. M. Bydder, "Ultrashort echo time imaging with bicomponent analysis," *Magnetic resonance in medicine*, vol. 67, pp. 645-649, 2012.
- [42] Wang, Z., Image quality assessment: from error visibility to structural similarity. *IEEE Transactions on Image Processing*, 2004. 13(4): p. 600.
- [43] Kingma, Diederik P., and Jimmy Ba. "Adam: A method for stochastic optimization." *arXiv preprint arXiv:1412.6980* (2014).
- [44] Kee Y, Sandino CM, Syed AB, Cheng JY, Shimakawa A, Colgan TJ, Hernando D, Vasanawala SS. Free-breathing mapping of hepatic iron overload in children using 3D multi-echo UTE cones MRI. *Magnetic Resonance in Medicine*.
- [45] Weiskopf, N. Weiskopf, A. Lutti, G. Helms, M. Novak, J. Ashburner, *et al.*, "Unified segmentation based correction of R1 brain maps for RF transmit field inhomogeneities (UNICORT)," *NeuroImage (Orlando, Fla. Print)*, vol. 54, pp. 2116-2124, 2011.
- [46] J. Ashburner and K. J. Friston, "Unified segmentation," *Neuroimage*, vol. 26, pp. 839-851, 2005.
- [47] S. Baudrexel, S. C. Reitz, S. Hof, R. M. Gracien, V. Fleischer, H. Zimmermann, *et al.*, "Quantitative T1 and proton density mapping with direct calculation of radiofrequency coil transmit and receive profiles from two-point variable flip angle data," *NMR in Biomedicine*, vol. 29, pp. 349-360, 2016.
- [48] N. Bloembergen, E. M. Purcell, and R. V. Pound, "Relaxation effects in nuclear magnetic resonance absorption," *Physical review*, vol. 73, p. 679, 1948.
- [49] West, Janne, J. B. M. Warntjes, and Peter Lundberg. "Novel whole brain segmentation and volume estimation using quantitative MRI." *European radiology* 22.5 (2012): 998-1007.
- [50] Wu Y, Li D, Xing L, Gold G. Deriving new soft tissue contrasts from conventional MR images using deep learning. *Magnetic Resonance Imaging*. 2020 Dec 1;74:121-7.
- [51] Pan SJ, Yang Q. A survey on transfer learning. *IEEE Transactions on knowledge and data engineering*. 2009 Oct 16;22(10):1345-59.
- [52] Kleesiek J, Morshuis JN, Isensee F, Deike-Hofmann K, Paech D, Kickingereder P, Köthe U, Rother C, Forsting M, Wick W, Bendszus M. Can virtual contrast enhancement in brain MRI replace gadolinium?: a feasibility study. *Investigative radiology*. 2019 Oct 1;54(10):653-60.
- [53] Narayana PA, Coronado I, Sujit SJ, Wolinsky JS, Lublin FD, Gabr RE. Deep learning for predicting enhancing lesions in multiple sclerosis from noncontrast MRI. *Radiology*. 2020 Feb;294(2):398-404.
- [54] Owraangi AM, Greer PB, Glide-Hurst CK. MRI-only treatment planning: benefits and challenges. *Physics in Medicine & Biology*. 2018 Feb 26;63(5):05TR01.
- [55] Xing L, Thorndyke B, Schreiber E, Yang Y, Li TF, Kim GY, Luxton G, Koong A. Overview of image-guided radiation therapy. *Medical Dosimetry*. 2006 Jun 1;31(2):91-112.
- [56] Moré, Jorge J. "The Levenberg-Marquardt algorithm: implementation and theory." *Numerical analysis*. Springer, Berlin, Heidelberg, 1978. 105-116.
- [57] O. Ronneberger, P. Fischer, and T. Brox, "U-net: Convolutional networks for biomedical image segmentation," in *International Conference on Medical Image Computing and Computer-Assisted Intervention*, 2015, pp. 234-241.
- [58] F. Milletari, N. Navab, and S.-A. Ahmadi, "V-net: Fully convolutional neural networks for volumetric medical image segmentation," in *2016 Fourth International Conference on 3D Vision (3DV)*, 2016, pp. 565-571.
- [59] Springenberg JT, Dosovitskiy A, Brox T, Riedmiller M. Striving for simplicity: The all convolutional net. *arXiv preprint arXiv:1412.6806*. 2014 Dec 21.
- [60] Huang G, Liu Z, Van Der Maaten L, Weinberger KQ. Densely connected convolutional networks. In *Proceedings of the IEEE conference on computer vision and pattern recognition* 2017 (pp. 4700-4708).
- [61] Hu, Xiaodan, et al. "RUNet: A robust UNet architecture for image super-resolution." *Proceedings of the IEEE/CVF Conference on Computer Vision and Pattern Recognition Workshops*. 2019.
- [62] K. He, X. Zhang, S. Ren, and J. Sun, "Deep residual learning for image recognition," in *Proceedings of the IEEE conference on computer vision and pattern recognition*, 2016, pp. 770-778.
- [63] K. He, X. Zhang, S. Ren, and J. Sun, "Identity mappings in deep residual networks," in *European conference on computer vision*, 2016, pp. 630-645.
- [64] M. Abadi, A. Agarwal, P. Barham, E. Brevdo, Z. Chen, C. Citro, *et al.*, "Tensorflow: Large-scale machine learning on heterogeneous distributed systems," *arXiv preprint arXiv:1603.04467*, 2016.
- [65] E. Gibson, W. Li, C. Sudre, L. Fidon, D. Shakir, G. Wang, *et al.*, "NiftyNet: a deep-learning platform for medical imaging," *arXiv preprint arXiv:1709.03485*, 2017.

[66] Lei Xing, Yan Wu. Qualitative and Quantitative MRI – a Simultaneous Acquisition of Qualitative and Quantitative MRI with the Support of Deep Learning

[67] Lei Xing, Yan Wu. Retrospective Tuning of Tissue Contrast in MRI for Precision Imaging